Chemical Science

ROYAL SOCIETY OF CHEMISTRY

EDGE ARTICLE

View Article Online
View Journal

Cite this: DOI: 10.1039/d2sc02768b

All publication charges for this article have been paid for by the Royal Society of Chemistry

Received 17th May 2022
Accepted 5th August 2022

DOI: 10.1039/d2sc02768b

rsc.li/chemical-science

Coherent ring-current migration of Mg-phthalocyanine probed by time-resolved X-ray circular dichroism†

Shichao Sun, * Haiwang Yong, Feng Chen and Shaul Mukamel *

The coherent ring current of Mg-phthalocyanine created by a broad band UV-visible pump pulse shows variation with time, where the ring currents at the corner benzene rings, around the Mg cation and on the outer ring oscillate with different time periods and the current density migrates among these regions. The 7 pairs of E_u degenerate excited states populated upon photoexcitation, generate 21 distinct coherent ring currents. We further calculate the time-resolved X-ray circular dichroism (TRXCD) spectrum of the coherences contributing to the ring current obtained by an attosecond X-ray probe pulse resonant with the nitrogen K-edge. A frequency domain TRXCD signal obtained by a Fourier transform of the signal with respect to the pump-probe delay time clearly separates the currents induced by different state pairs.

Controlling and measuring attosecond movements of electrons in molecules are of fundamental importance for photoinduced chemical reactions. Ring current, a circular electron motion, can be induced in cyclic conjugated molecules by applying a static magnetic field,[1–10] by using circularly polarized light (CPL)[11] or by coupling the molecule to an optical chiral cavity.[12] Magnetic-field-induced ring currents are widely applied in nuclear magnetic resonance,[8,13–15] where a static field non-resonant with electronic excited states perturbs the ground state and creates a ground state ring current. The direction of the magnetic field induced current is determined by the direction of the applied magnetic field and the aromaticity of the molecule, where aromatic (antiaromatic) molecules produce diamagnetic (paramagnetic) ring currents.[1,2,16–19]

In this theoretical study, we focus on the CPL induced ring currents, which are receiving considerable attention.[11,20–34] The sense of the resulting ring current is determined by the circular polarization of the pulse. Furthermore, CPL can create ring currents in selected states by tuning the pulse frequency to specific electronic states. This offers an additional control over the ring current generation.

We consider a molecule with two excited states with perpendicular transition dipoles to the ground state. We denote the excited states $|E_x\rangle$ and $|E_y\rangle$, whose transition dipole $\langle g|\boldsymbol{\mu}|E_{x,y}\rangle$ are along the x and y direction respectively. If the bandwidth of the circularly polarized pulse with polarization $\boldsymbol{\varepsilon}_\pm = \frac{\boldsymbol{\varepsilon}_x \pm i\boldsymbol{\varepsilon}_y}{2}$ covers both states, the pulse will excite them with a phase difference of $\frac{\pi}{2}$, giving the electron oscillation in x and y direction a $\frac{\pi}{2}$ phase difference, thus driving the electrons to move in a circle.[11]

If this pair of excited states is degenerate, by a linear combination, we can create a pair of degenerate current-carrying eigenstates $|E_\pm\rangle = \frac{|E_x\rangle \pm i|E_y\rangle}{\sqrt{2}}$.[11,30] A circularly polarized $\boldsymbol{\varepsilon}_\pm$ light pulse increases the population of state $|E_\pm\rangle$ respectively. Thus, the ring current created by the pulse can be viewed as population ring current which remains time-independent after the pump pulse is over. If the excited state pair is non-degenerate, the ring current is proportional to their coherence and is denoted coherent ring current.[24,25,35] After the pulse is over, the population is stationary while the coherent ring current oscillates with a period inversely proportional to the energy difference between the coherent states.

Previous research on coherent ring currents had focused on a single pair of coherence, where the current of the entire molecule evolves with the same pace.[11,20–26,28–30] Here, we study the ring-current dynamics resulting from the superposition of multiple ring-current pairs created by a broad band circularly pump pulse. Due to the interplay of multiple coherences, we find that the evolution of ring current at different locations in the molecule show distinct feature. As the coherent current density evolves with time, we see the redistribution of current density between different regions of the molecule, which can be viewed as current migration. This behavior is analogous to the

Department of Chemistry and Department of Physics & Astronomy, University of California, Irvine, USA. E-mail: shichas2@uci.edu; smukamel@uci.edu

† Electronic supplementary information (ESI) available: Coherent ring-current dynamics of Mg-phthalocyanine probed by time-resolved circular dichroism. See https://doi.org/10.1039/d2sc02768b

light-induced charge migration and the following evolution of electrons.[36,37,54] Localized ring currents created at different regions within the molecule, create new possibilities for designing molecular device.[38]

We focus on phthalocyanine which has broad applications in *e.g.* dye-sensitized solar cells[39,40] and photosensitizers for cancer photodynamic therapy.[41] Its derivative Mg-phthalocyanine (MgPc) has a rigid structure (see Fig. 1), which remains stable during the electronic dynamics.[42,43] MgPc has a high density of states belonging to the E_u irreducible representation (Table S1†), which facilitates the coherent excitation of many excited states. The molecule has multiple rings, including a central ring and the four benzene rings in the corners, which makes it possible to observe the dynamics of both local and global ring currents. We use a broadband UV pump pulse with 2 eV bandwidth made possible by recently developed attosecond UV-visible pulses.[44] Upon excitation, 7 pairs of degenerate excited states are populated within the pulse bandwidth to create 21 coherence pairs. These coherent ring currents have different profiles, giving rise to distinct evolution of local and the global ring currents. We further show that these coherences can be observed in time-resolved X-ray circular dichroism (TRXCD) spectrum resonant to the nitrogen K-edge. Contributions from each ring-current pair can be clearly identified in the Fourier-transformed CD spectrum.

As illustrated in Fig. 1, a circularly polarized pump pulse $\mathscr{E}_{\text{left}}(t) = E_0[\mathbf{e}_x \cos(\Omega(t)) - \mathbf{e}_y \sin(\Omega(t))]\exp\left[-\frac{t^2}{2\tau_{\text{pu}}{}^2}\right]$ propagating along z perpendicular to the molecular x–y plane with an amplitude of 6.9934×10^9 V m^{-1}, central frequency $\Omega = 4.0$ eV and duration of $\tau_{\text{pu}} = 4.64$ fs is applied at 0 fs to generate a ring current. The pulse duration and amplitude are chosen to excite 91.5% of the ground state population to excited states (Fig. S2†), thus create a high excited state population in this multi-level system. The mechanism is similar to Rabi-flop of two-level system. The electronic wave function is obtained by numerically solving the time-dependent Schrödinger equation $i\frac{\partial|\psi(t)\rangle}{\partial t} = [H_{\text{mol}} - \boldsymbol{\mu}\cdot\mathscr{E}_{\text{left}}(t)]|\psi(t)\rangle$, where H_{mol} is the molecular Hamiltonian and the wave function is expanded in the molecular ground and valence excited states basis $|\psi(t)\rangle = \sum_{\text{A}} a_{\text{A}}(t)|\text{A}\rangle$. Atomic units are used throughout. MgPc belongs to the D_{4h} point group. Its excited states are obtained by a TDDFT calculation. The molecular geometry is optimized using DFT with the B3LYP functional[45–48] and the 6-31g(d) basis set and Gaussian 16.[49] Both valence and core excited states are computed with TDDFT in the Tamm–Dancoff approximation (TDA) using the Chronus Quantum software package.[50] The TDA calculations employ the same density functional and basis set used in the geometry optimization. The valence excited states are listed in Table S1.† For CPL with circularly polarization in x–y plane, the excited states of E_u irreducible representation with two-fold degeneracy are dipole allowed, and denoted mE_ux and mE_uy, where x, y denote the transition dipole direction, and m, $n = 1$, 2, …, 7 is the index of pair of degenerate states. The state with A_{2u} irreducible representation has transition dipole $\langle g|\boldsymbol{\mu}|e\rangle$ along z and is thus not excited by the pump pulse. The current density is given by[51]

$$\mathbf{j}(\mathbf{r},\mathbf{t}) = \sum_{\text{A,B}} D_{\text{BA}}(\mathbf{t})\mathbf{j}_{\text{AB}}(\mathbf{r}) \tag{1}$$

$$\mathbf{j}_{\text{AB}}(\mathbf{r}) = \sum_{\mu\nu} D^{\text{BA}}_{\nu\mu}\left(\chi^*_\mu(\mathbf{r})\nabla\chi_\nu(\mathbf{r}) - \nabla\chi^*_\mu(\mathbf{r})\chi_\nu(\mathbf{r})\right) \tag{2}$$

where A, B run over the ground and valence excited states, $D_{\text{BA}}(t) = a^*_{\text{A}}(t)a_{\text{B}}(t)$ is the density matrix at time t, $a_{\text{B}}(t)$ is the coefficient of electronic states. $D^{\text{BA}}_{\nu\mu}$ is the transition one-electron density matrix (1PDM) between electronic state B and A in the atomic orbital basis and νμ denote atomic orbital. $\chi_\mu(\mathbf{r})$ and $\nabla\chi_\mu(\mathbf{r})$ are the atomic orbital basis and its gradient respectively.

The induced ring current is further probed by the TRXCD signal at the nitrogen K-edge. The Gaussian X-ray probe pulse has central frequency $\omega_c = 383.172$ eV, $\sigma = 0.7$ fs and time delay T scanned from 0 to 25 fs. The TRXCD signal is derived in ESI S1† using time dependent perturbation theory in the probe pulse–molecule interaction

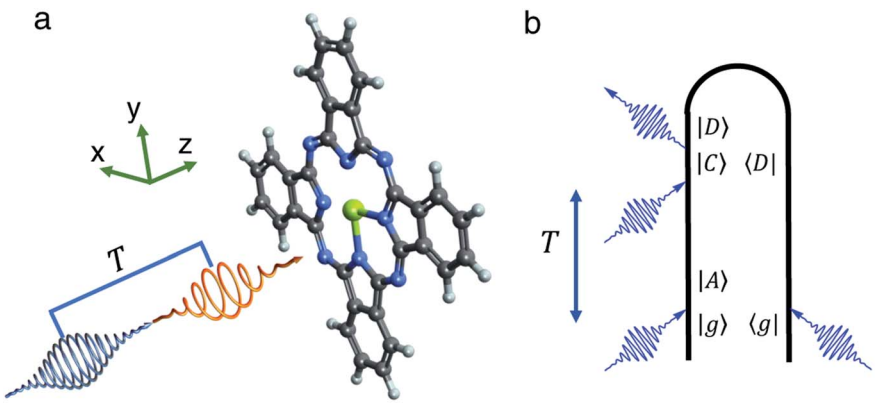

Fig. 1 (a) Sketch of the pump probe experiment. Mg-Pc is pumped by a circularly polarized UV-visible short pulse (orange arrow) and creates a coherent ring current. The coherence is detected by the TRXCD signal using an X-ray probe pulse (blue arrow) with a time delay T. (b) Loop diagram of X-ray TRXCD. Only the excited state absorption contribution is relevant to our study.

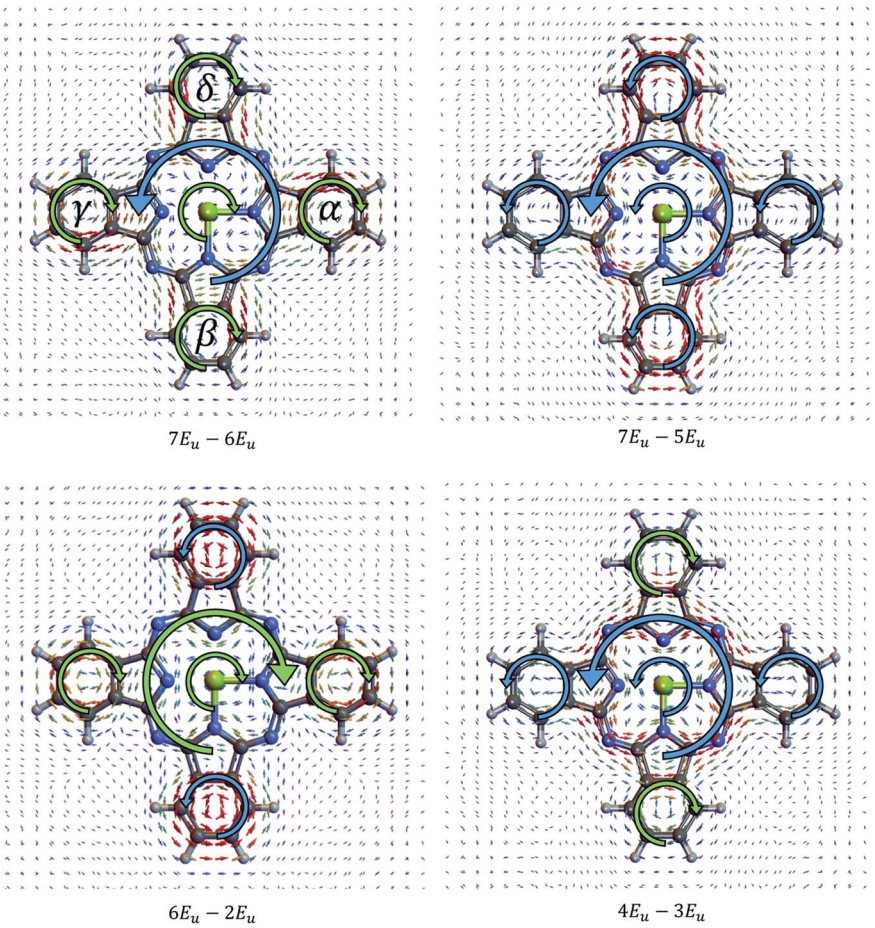

Fig. 2 Current density of the coherence between pair $7E_u$–$6E_u$, $7E_u$–$5E_u$, $6E_u$–$2E_u$, $4E_u$–$3E_u$ respectively. Counter-clockwise local current directions are marked with big thick blue arrows while clockwise local current directions are marked with thick light green arrows.

$$S_{\mathrm{TRXCD}}(\omega, T) = 2\sqrt{2\pi}\sigma\ \mathrm{Re}\left\{ \sum_{\mathrm{A,D=g,val C=core}} \sum \frac{\mathbf{j}_{\mathrm{DC}}(\mathbf{k}) \times \mathbf{j}^{\dagger}_{\mathrm{CA}}(-\mathbf{k})}{\omega_{\mathrm{DC}} + \omega + i\Gamma} \cdot \boldsymbol{\varepsilon}_{\kappa} \int_0^{+\infty} \mathrm{d}t\ \mathrm{e}^{i(\omega-\omega_{\mathrm{c}})(t-T)}\ \mathrm{e}^{-\frac{1}{2}\left[\frac{(t-T)^2}{\sigma^2}+\sigma^2(\omega-\omega_{\mathrm{c}})^2\right]} a^{*}_{\mathrm{D}}(t) a_{\mathrm{A}}(t) \right\} \quad (3)$$

where A, D run over the ground and valence excited states and C denotes core excited states. We employed the minimal coupling Hamiltonian for calculating the CD signal, where the transition current density is used in the CD expression instead of multipole moments.[51,52] The minimal coupling expression includes implicitly the contributions to all orders of multipolar moments.[51,52] Since CPL induces ring current only for oriented molecule,[20] the TRXCD signal is simulated for oriented molecules. $\boldsymbol{\varepsilon}_{\kappa}$ is the propagation unit vector of the probe pulse, and $\mathbf{k} = \frac{\omega}{c}\boldsymbol{\varepsilon}_{\kappa}$. $\mathbf{j}_{\mathrm{DC}} = \int \mathrm{d}\mathbf{r}\, \mathbf{j}_{\mathrm{DC}}(\mathbf{r})\mathrm{e}^{-i\mathbf{k}\cdot\mathbf{r}}$ is the momentum space transition current density. ω_{DC} is the transition energy from state C to D. ω is the angular frequency. $\Gamma = 0.093$ eV is core line width for nitrogen.[53] Here we focus on the nitrogen K-edge since the Mg line width ($\Gamma = 0.45$ eV)[53] is too broad to resolve different excited states as shown in Fig. S2.†

Ring current migration and the corresponding excited state coherences

The ring-currents formed by a pair of degenerate states populations, for example the mE_u reach a stationary value after the pulse is over. Ring-currents can also be formed by the coherence between states which belong to different degenerate pairs, for example, the coherence $mE_u x$–$nE_u y$, where $m \neq n$. This coherence oscillates in time with the period $\frac{2\pi}{|\omega_{mE_u, nE_u}|}$.

During the pulse, the ground/excited state (g–ex) coherence makes a large contribution to the current. When the pulse is switched off, the coefficient of ground state is small, thus the fast oscillatory component of induced ring current becomes weaker as shown in Fig. S4.† Since the oscillation is faster than the probe pulse duration, the g–ex coherence is not resolved by the TRXCD signal. We thus focus on the excited state-excited state (ex–ex) coherences, which contribute to slower components of the ring current.

The ring currents associated with different ex–ex coherence pairs $\mathbf{j}_{AB}$ have distinct spatial profiles. Ring currents can arise in four zones in the MgPc molecule. First is in the center around Mg cation denoted "CT", second is the current on the outer ring denoted "OT", third is the current on the right and left benzene rings denoted "α" and "γ" respectively, fourth is the lower and upper benzene rings labelled "β" and "δ" respectively, as shown in Fig. 2. Currents associated with several pairs of states are shown in Fig. 2. For the same coherence, the ring current at different locations can have a different direction. For example, the $7E_u$–$5E_u$ coherent ring current has the same direction around the Mg (CT) and on the outer loop (OT), while for the $7E_u$–$6E_u$ current, the direction of CT and OT are opposite. The direction of the α, γ and β, δ ring currents are the same in $7E_u$–$5E_u$ and $7E_u$–$6E_u$, while in $6E_u$–$2E_u$ and $4E_u$–$3E_u$, the α, γ and β, δ have opposite direction.

As each component of the coherent ring current $\mathbf{j}_{mE_u,nE_u}$ oscillates with its own period of $\frac{2\pi}{|\omega_{mE_u,nE_u}|}$, the total induced ring current varies with time, where the current evolutions at different locations is unsynchronized. This behavior is different from the ring current induced by narrow band pump,[35] where the ring current in the entire molecule oscillates uniformly.

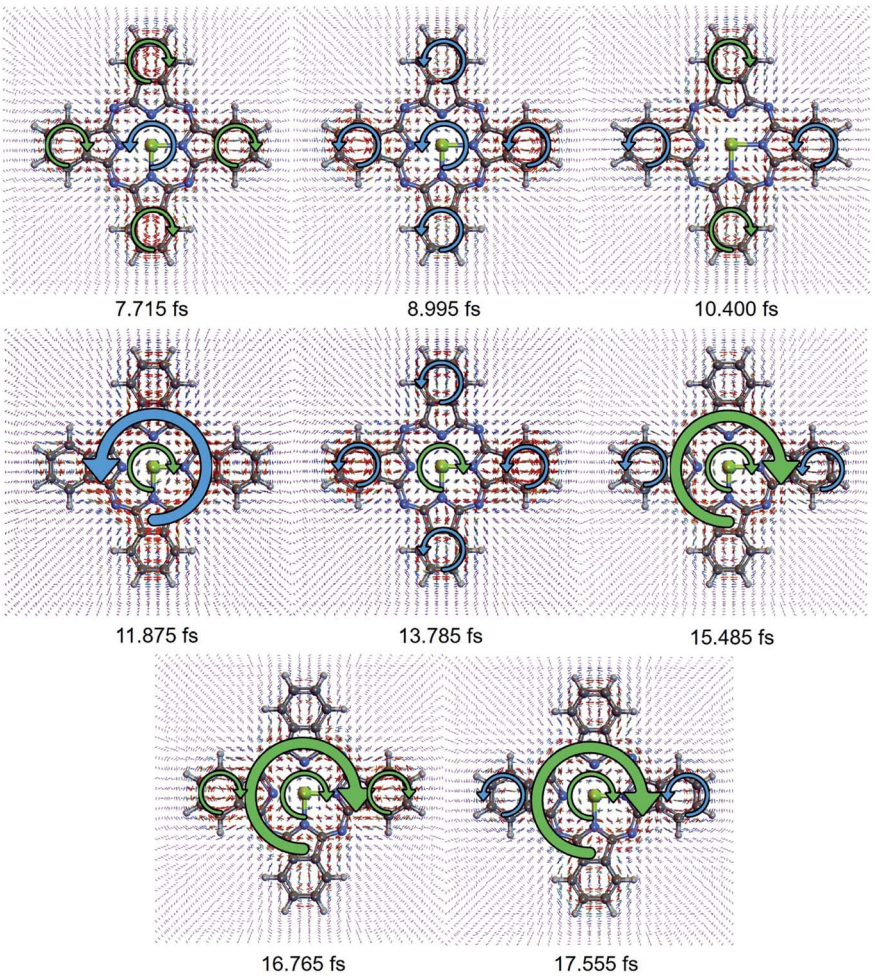

Fig. 3 Snapshots of the total ex–ex ring current at different times after the pump. The ring current direction is marked by a green arrow (clockwise) and blue arrow (counter-clockwise) respectively. From 7.715 fs to 8.995 fs, the current on the outer four benzene rings change from clockwise to counter-clockwise while the current around Mg atom (CT) is unchanged. From 8.995 fs to 10.400 fs, the ring currents on the upper and lower corner rings (β, δ) change to clockwise, while the CT ring current disappear. Then at 11.875 fs, the ring currents around four small corner rings disappear, while the counter-clockwise outer ring current (OT) and clockwise CT ring current appears. Then at 13.785 fs, the counter-clockwise ring current around four corner rings appear, while the OT ring current disappear, and the clockwise CT ring current remain intact. At 15.485 fs, the clockwise OT ring current is formed while the counter-clockwise current in the β, δ ring disappear. At 16.765 fs, the current at left and right corner ring change from counter-clockwise to clockwise, and then change back to counter-clockwise at 17.555 fs.

This unsynchronized evolution of currents at different zones causes the redistribution of current density, resulting in the current migration in the whole molecule. The total ex–ex coherent ring current profile at various time delays T after CPL are depicted in Fig. 3. We show the local ring current profiles at the four corner benzene rings (α, γ and β, δ), the center zone around Mg (CT), and the outer loop of the total molecule (OT) reverse direction at different times. For example, at 7.715 fs, α, γ and β, δ are clockwise whereas CT is counter-clockwise. At 8.995 fs, all currents are counter-clockwise. Between 7.715 fs and 8.995 fs, α, γ and β, δ change from clockwise to counter-clockwise while CT is unchanged. From 8.995 fs to 10.400 fs, the β, δ change to clockwise, while CT vanishes. Moving to 11.875 fs, the ring current around α, γ and β, δ disappear, while a counter-clockwise OT ring current and clockwise ring current CT appear. Then at 13.785 fs, counter-clockwise currents α, γ and β, δ rings appear, the OT ring current disappears, and the clockwise ring current CT remains intact. At 15.485 fs, the clockwise current OT is formed while the counter-clockwise current in the β, δ current vanishes. At 16.765 fs, the current α, γ changes from counter-clockwise to clockwise, and then changes back to counter-clockwise at 17.555 fs.

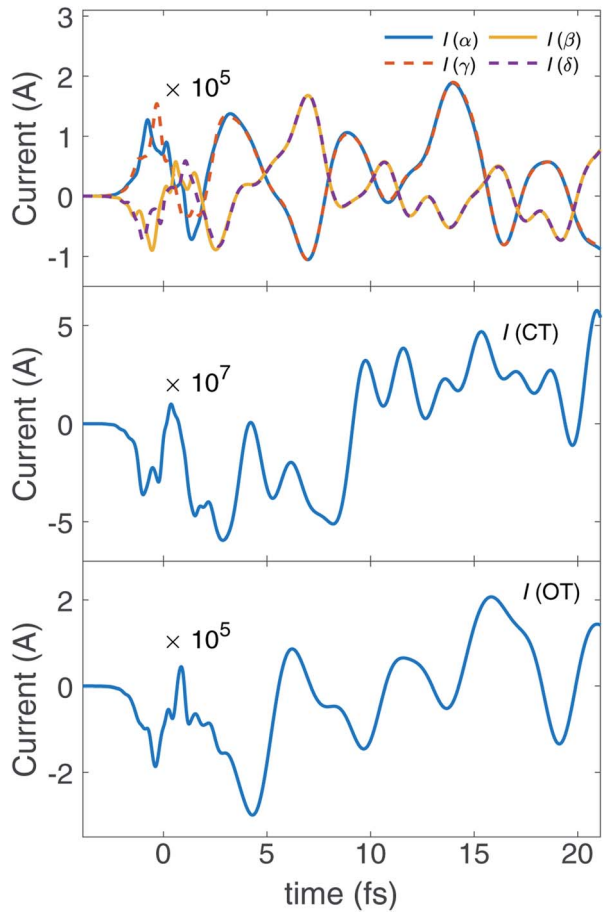

Fig. 4 Time evolution of local ring current induced by excited state-excited state coherence. From top to bottom, the plots are ring currents of the four corner benzene rings (α, β, γ and δ ring), around the Mg atom at center (CT) and the outer ring (OT). Currents in Ampere are calculated by numerically integrating the current density at a plane, as illustrated in Fig. S8.† Positive values of currents indicate clockwise ring current. After the pump pulse, the currents of γ/δ are identical to α/β. We can clearly see the currents migrate between ring αγ and βδ.

The time evolution of the local ring currents is plotted in Fig. 4. The currents in ampere are calculated by integrating the current density on a plane. Details of the integration are explained in ESI S9.† After the pump pulse, the corner rings at opposite position (like α, γ and β, δ) have the same ring current rotation direction, while neighboring rings have no such relationship. This is due to the fact that these coherent ring currents are generated by excited states with E_u irreducible representation whose $\mathbf{j}_{mE_u,nE_u}$ are invariant under C_2 rotation with respect to the principle axis. We can clearly see the transfer of ring currents among the four corner rings, between {α, γ} and {β, δ}. Overall, Fig. 4 depicts the unsynchronized evolution of the current at four different zones (CT, OT, α, γ and β, δ). The redistribution of ring currents among these zones results in ring current migration dynamics.

In summary, the coherent ring current induced by a broad band pump pulse for a multi-ring molecule can change its direction and magnitude locally, in contrast to changing the total ring current direction globally when a narrow band pulse is applied. The ring current migration among different zones in the molecule is caused by the interplay of multiple pairs of coherent ring currents. The directions and strengths of induced ring current result in an induced magnetic field, computed with Biot–Savart law, as displayed in Fig. S4 and S5.† The induced magnetic field is further decomposed into the contributions of different coherences.

The time-resolved circular dichroism signal at the K-edge

For the time domain TRXCD signal $S(\omega,T)$ in the upper panel of Fig. 5, peaks are located where ω coincides with valence to a core excitation energy ω_{CD}. The peak intensity is proportional to the numerator $\mathbf{j}_{DC} \times \mathbf{j}^{\dagger}_{CA}$ of eqn (3) and the coherence $a^{*}_{D}a_{A}$. To assign each peak to a valence-core excitation, we take a vertical slice of the spectrum at time 10.40 fs from the TRXCD and identify important valence to core state transitions as described in ESI.†

The time dependence of the TRXCD signal arises from the coherence between E_u states. To separate the signals with different oscillation period, we perform a Fourier transform of the time domain TRXCD signal $S(\omega,T)$ with respect to the delay time T which results in the frequency domain signal $\tilde{S}(\omega,\omega')$. Since the pump pulse is centered at 0 fs, the pump pulse driven part of the TRXCD spectrum is eliminated by taking the Fourier transform for the TRXCD in the 3.72 fs to 21.10 fs interval. The Fourier transformed CD spectra as a function of the oscillation frequency ω' and excitation energy $\hbar\omega$ is depicted in the lower panel of Fig. 5. The $\hbar\omega'$ value of the bright colored peaks indicates the energy difference of the coherent states, which coincides with oscillation angular frequency of the coherence. Table 1 lists the coherences as well as their oscillation frequencies.

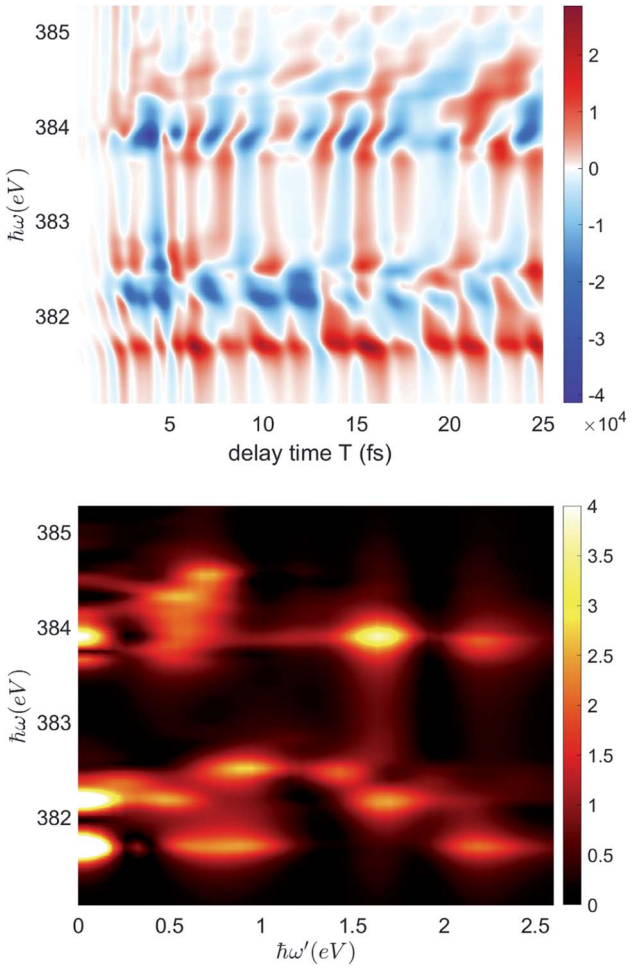

Fig. 5 Upper panel: Simulated nitrogen K-edge X-ray TRXCD signal eqn (3). The delay time T is scanned from 0 fs to 25 fs. The intensity of the signal is in arbitrary units. Lower panel: Fourier transformed circular dichroism spectrum of nitrogen K-edge. $\hbar\omega$ is detection frequency and $\hbar\omega'$ is the conjugate variable of delay time T. For each bright peak, the $\hbar\omega$ is the excitation energy and the $\hbar\omega'$ values indicate the frequency of oscillation corresponding to the coherence contributing to the peak.

The CD signal at peak energies and the corresponding coherence frequencies

We first consider the peaks for $\hbar\omega' = 0$ in the lower panel of Fig. 5, which originate from the time independent population ring current. The peaks at $\hbar\omega = 381.6788$, 383.669, 383.8017 eV represent the population ring current of $7E_u$, with excitation to core states 7, 23, 25 respectively (see ESI S2† for the labels of core excited states).

The remaining peaks correspond to coherent ring currents. $\hbar\omega'$ indicates the energy gap between the coherent states, resolved in Fig. 5, with both energy gaps of the coherent states and the coherence frequency obtained from the peaks listed in Table 1. The coherence pairs with a similar energy gap can be separated by different core state excitation energy $\hbar\omega$, for example, $4E_u$–$1E_u$ and $5E_u$–$1E_u$. Such separation can be achieved for the nitrogen K-edge but not in the Mg K-edge due to its large line width.[53] With the aid of ω and ω', each peak in Fig. 5 assigned to a coherence with its valence to core transitions is listed in Table 1.

The coherence with longest period is $4E_u$–$3E_u$ with an energy difference of 0.1023 eV. It contributes to the peak at $\hbar\omega = 382.4157$ eV with coherence frequency $\hbar\omega' = 0.2377$ eV. Since the total simulation time is kept short to avoid decoherence, the $4E_u$–$3E_u$ coherence did not complete a single period, which causes the deviation of ω' from the energy difference.

The brightest peak at $\hbar\omega' = 1.6374$ eV and $\hbar\omega = 383.9051$ eV corresponds to the excitation from $1E_u$ to core state 7, contributed by $5E_u$–$1E_u$ coherence.

At $\hbar\omega' = 0.5354$ eV, the peaks with excitation energy between 383.6 and 384.5 eV correspond to the transition from $7E_u$ and $5E_u$ to different core excited states, contributed by the $7E_u$–$5E_u$ coherence. The peaks at $\hbar\omega = 384.2041$, 384.3369 eV represent the excitation from $5E_u$ to core state 22 and 25 respectively; peak at 383.669 eV and 383.8017 are excitation from $7E_u$ to core state 22 and state 25 respectively.

Decoherence effects

The ring current is expected to decay due to the interaction of electronic system with a nuclear bath. Such dephasing effects are not included in the Schrödinger equation, but can be described phenomenologically. Pure dephasing can be included by (1) multiplying the signal expression eqn (3) by a dephasing factor $e^{-\Gamma_{1,DA}\tau}$, where $\Gamma_{1,DA}$ is the valence–valence coherence dephasing rate and (2) add a term $i\Gamma_{2,DC}$ to the denominator of eqn (3) as given in the ESI.† In Section S8,† the TRXCD spectra and the Fourier transformation are shown for different values of dephasing rates, *i.e.*, from 1/100 fs^{-1} to 1/10 fs^{-1} (Fig. S7†). The valence states-core states dephasing broadens the peak in energy domain $\hbar\omega$. Since the dephasing rate contribution is less than the lifetime broadening of core excited states, this effect is not significant. The valence excited state-valence excited state dephasing causes a decay of the TRXCD signal with the delay time T. Higher dephasing rates result in earlier decay of TRXCD signal in time domain, as well as lower resolution in frequency domain $\hbar\omega'$. Nevertheless, distinct coherence components can still be assigned in the Fourier transformed spectrum even with a high dephasing rate of 1/10 fs^{-1}. The dephasing of ground state–valence excited state does not affect the TRXCD signal, since such coherence has shorter oscillation period than the probe pulse duration, thus not observed in the signal. In summary, although dephasing of coherence results in lower resolution of the spectra, it does not change peak assignments.

Apart from dephasing, the coherence of excited states can cause magnetic dipole radiation, since the transition magnetic dipoles between excited state of E_u irreducible representation are nonzero while their transition electric dipoles vanish. This radiation causes damping of excited states. However, since the magnetic dipole radiation is weak, this effect is ignored in our simulation.

In conclusion, a broad band (2 eV) UV-visible circularly polarized pump pulse is used in this study to create a superposition of 7 degenerate pairs of excited states. The coherent ring

Table 1 The coherence contributing to the TRXCD spectrum including the energy difference of the coherent states as well as coherence frequency $\hbar\omega'$ obtained from the x-axis value of the bright peaks in Fig. 5

Coherence	Period (fs)	Energy difference (eV)	Coherence frequency $\hbar\omega'$ (eV)	Excitation energy $\hbar\omega$ (eV)	Transition valence to core
$4E_u$–$3E_u$	40.427	0.1023	0.2377	382.4157	$4E_u$ to core states 6
$7E_u$–$6E_u$	8.545	0.4840	0.4666	382.1627	$6E_u$ to core state 7, 8
$7E_u$–$5E_u$	7.726	0.5353	0.5354	384.2041	$5E_u$ to core state 22
				384.3369	$5E_u$ to core state 25
				383.6690	$7E_u$ to core state 22
				383.8017	$7E_u$ to core state 25
$7E_u$–$3E_u$	4.929	0.8391	0.8798	381.6788	$7E_u$ to core state 7, 8
				382.5179	$3E_u$ to core state 6
$4E_u$–$1E_u$	2.776	1.4896	1.4308	382.4157	$4E_u$ to core states 6
$5E_u$–$1E_u$	2.446	1.6911	1.6374	383.9051	$1E_u$ to core state 7
$6E_u$–$1E_u$	2.374	1.7424	1.7063	381.6788	$7E_u$ to core state 7, 8
				382.1627	$6E_u$ to core state 7, 8
$7E_u$–$1E_u$	1.858	2.2264	2.1884	383.9051	$1E_u$ to core state 7

currents at different locations in the molecule show distinct features, where the coherent ring current on the corner rings, outer ring and inner ring around the Mg evolve unsynchronizedly due to the interplay of many coherence pairs of Mg-Pc excited states. This coherence may be probed by time-resolved X-ray circular dichroism spectrum at the nitrogen K-edge. By Fourier transforming the CD signal with respect to the probe delay time T, we obtain the CD spectrum as a function of excitation energy and oscillation frequency. Bright peaks are assigned to pairs of excited state coherence by the coherence frequency and its excitation energy in the two dimensional spectrum Fig. 5. This suggests a way to probe the evolution of ring current in time domain and separate individual excited state coherence contributing to the coherent ring current in the frequency domain. The redistribution of current density within the molecule pave the way for controlling the local electron movement within the molecule, enabling light control of electron at sub-molecular scale and femtosecond time scale.

Data availability

All study data are included in the article and/or ESI.†

Author contributions

S. M. supervised and conceived the project. S. S. and F. C. derived the equations for the signal. S. S. performed the electronic structure calculations. S. S., F. C. and H. Y. performed spectroscopy simulations. All authors contributed to the analysis and interpretation of the results, and wrote the manuscript.

Conflicts of interest

There are no conflicts to declare.

Acknowledgements

The support of the National Science Foundation through Grant No. CHE-1953045 is gratefully acknowledged. S. M. was supported by the U.S. Department of Energy, Office of Science, Office of Basic Energy Sciences under Award DE-FG02-04ER15571. S. M. is a fellow of the Hagler Institute for Advanced Study at Texas A&M University.

References

1 F. London, Théorie quantique des courants interatomiques dans les combinaisons aromatiques, *J. Phys. Radium*, 1937, **8**, 397–409.
2 R. Breslow, Antiaromaticity, *Acc. Chem. Res.*, 1973, **6**, 393–398.
3 P. Lazzeretti, Ring Currents, *Prog. Nucl. Magn. Reson. Spectrosc.*, 2000, **36**, 1–88.
4 J. Jusélius and D. Sundholm, The Aromatic Character of Magnesium Porphyrins, *J. Org. Chem.*, 2000, **65**, 5233–5237.
5 E. Steiner and P. W. Fowler, Patterns of Ring Currents in Conjugated Molecules: A Few-Electron Model Based on Orbital Contributions, *J. Phys. Chem. A*, 2001, **105**, 9553–9562.
6 G. Merino, T. Heine and G. Seifert, The Induced Magnetic Field in Cyclic Molecules, *Chem.–Eur. J.*, 2004, **10**, 4367–4371.
7 E. Steiner, A. Soncini and P. W. Fowler, Ring Currents in the Porphyrins: π Shielding, Delocalisation Pathways and the Central Cation, *Org. Biomol. Chem.*, 2005, **3**, 4053–4059.
8 T. Heine, C. Corminboeuf and G. Seifert, The Magnetic Shielding Function of Molecules and Pi-Electron Delocalization, *Chem. Rev.*, 2005, **105**, 3889–3910.
9 B. Kudisch, M. Maiuri, L. Moretti, M. B. Oviedo, L. Wang, D. G. Oblinsky, R. K. Prud'homme, B. M. Wong, S. A. McGill and G. D. Scholes, Ring Currents Modulate Optoelectronic Properties of Aromatic Chromophores at 25 T, *Proc. Natl. Acad. Sci. U. S. A.*, 2020, **117**, 11289–11298.
10 M. D. Peeks, T. D. Claridge and H. L. Anderson, Aromatic and Antiaromatic Ring Currents in a Molecular Nanoring, *Nature*, 2017, **541**, 200–203.
11 I. Barth, J. Manz, Y. Shigeta and K. Yagi, Unidirectional Electronic Ring Current Driven by a Few Cycle Circularly Polarized Laser Pulse: Quantum Model Simulations for

Mg- porphyrin, *J. Am. Chem. Soc.*, 2006, **128**, 7043–7049, PMID: 16719485.
12 S. Sun, B. Gu and S. Mukamel, Polariton Ring Currents and Circular Dichroism of Mg-porphyrin in a Chiral Cavity, *Chem. Sci.*, 2022, **13**, 1037–1048.
13 L. Jackman, F. Sondheimer, Y. Amiel, D. Ben-Efraim, Y. Gaoni, R. Wolovsky and A. Bothner-By, The Nuclear Magnetic Resonance Spectroscopy of a Series of Annulenes and Dehydro-Annulenes, *J. Am. Chem. Soc.*, 1962, **84**, 4307–4312.
14 R. H. Mitchell, Measuring Aromaticity by NMR, *Chem. Rev.*, 2001, **101**, 1301–1316, PMID: 11710222.
15 A. D. Allen and T. T. Tidwell, Antiaromaticity in Open-Shell Cyclopropenyl to Cycloheptatrienyl Cations, Anions, Free Radicals, and Radical Ions, *Chem. Rev.*, 2001, **101**, 1333–1348.
16 L. Pauling, The Diamagnetic Anisotropy of Aromatic Molecules, *J. Chem. Phys.*, 1936, **4**, 673–677.
17 J. Pople, Proton Magnetic Resonance of Hydrocarbons, *J. Chem. Phys.*, 1956, **24**, 1111.
18 J. Pople and K. Untch, Induced Paramagnetic Ring Currents, *J. Am. Chem. Soc.*, 1966, **88**, 4811–4815.
19 J. Gomes and R. Mallion, Aromaticity and Ring Currents, *Chem. Rev.*, 2001, **101**, 1349–1384.
20 I. Barth and J. Manz, Periodic Electron Circulation Induced by Circularly Polarized Laser Pulses: Quantum Model Simulations for Mg Porphyrin, *Angew. Chem., Int. Ed.*, 2006, **45**, 2962–2965.
21 I. Barth and J. Manz, Electric Ring Currents in Atomic Orbitals and Magnetic Fields Induced by Short Intense Circularly Polarized π Laser Pulses, *Phys. Rev. A: At., Mol., Opt. Phys.*, 2007, **75**, 012510.
22 I. Barth, J. Manz and L. Serrano-Andrés, Quantum Simulations of Toroidal Electric Ring Currents and Magnetic Fields in Linear Molecules Induced by Circularly Polarized Laser Pulses, *Chem. Phys.*, 2008, **347**, 263–271, Ultrafast Photoinduced Processes in Polyatomic Molecules.
23 M. Kanno, H. Kono, Y. Fujimura and S. H. Lin, Nonadiabatic Response Model of Laser-Induced Ultrafast π-Electron Rotations in Chiral Aromatic Molecules, *Phys. Rev. Lett.*, 2010, **104**, 108302.
24 H. Mineo, M. Yamaki, Y. Teranishi, M. Hayashi, S. H. Lin and Y. Fujimura, Quantum Switching of π-Electron Rotations in a Nonplanar Chiral Molecule by Using Linearly Polarized UV Laser Pulses, *J. Am. Chem. Soc.*, 2012, **134**, 14279–14282.
25 M. Kanno, Y. Ono, H. Kono and Y. Fujimura, Laser-Polarization Effects on Coherent Vibronic Excitation of Molecules with Quasi-Degenerate Electronic States, *J. Phys. Chem. A*, 2012, **116**, 11260–11272, PMID: 22834970.
26 H. Mineo, S. Lin and Y. Fujimura, Coherent π-Electron Dynamics of (P)-2,2′-biphenol Induced by Ultrashort Linearly Polarized UV Pulses: Angular Momentum and Ring Current, *J. Chem. Phys.*, 2013, **138**, 074304.
27 H. Mineo, S. Lin and Y. Fujimura, Vibrational Effects on UV/Vis Laser-Driven π-Electron Ring Currents in Aromatic Ring Molecules, *Chem. Phys.*, 2014, **442**, 103–110.
28 J. J. Rodriguez and S. Mukamel, Probing Ring Currents in Mg-Porphyrins by Pump–Probe Spectroscopy, *J. Phys. Chem. A*, 2012, **116**, 11095–11100, PMID: 22881200.
29 K.-J. Yuan, C.-C. Shu, D. Dong and A. D. Bandrauk, Attosecond Dynamics of Molecular Electronic Ring Currents, *J. Phys. Chem. Lett.*, 2017, **8**, 2229–2235, PMID: 28468499.
30 M. Kanno, H. Kono and Y. Fujimura, Laser-Control of Ultrafast π-Electron Ring Currents in Aromatic Molecules: Roles of Molecular Symmetry and Light Polarization, *Appl. Sci.*, 2018, **8**, 2347.
31 K. R. Nandipati and O. Vendrell, On the Generation of Electronic Ring Currents under Vibronic Coupling Effects, *J. Chem. Phys.*, 2020, **153**, 224308.
32 K. R. Nandipati and O. Vendrell, Dynamical Jahn-Teller effects on the generation of electronic ring currents by circularly polarized light, *Phys. Rev. Res.*, 2021, **3**, L042003.
33 S. Eckart, *et al.*, Ultrafast Preparation and Detection of Ring Currents in Single Atoms, *Nat. Phys.*, 2018, **14**, 701–704.
34 O. Neufeld and O. Cohen, Background-Free Measurement of Ring Currents by Symmetry-Breaking High-Harmonic Spectroscopy, *Phys. Rev. Lett.*, 2019, **123**, 103202.
35 Y. Nam, J. R. Rouxel, J. Y. Lee and S. Mukamel, Monitoring Aromatic Ring-Currents in Mg-Porphyrin by Time-Resolved Circular Dichroism, *Phys. Chem. Chem. Phys.*, 2020, **22**, 26605–26613.
36 H. J. Wörner, C. A. Arrell, N. Banerji, A. Cannizzo, M. Chergui, A. K. Das, P. Hamm, U. Keller, P. M. Kraus, E. Liberatore, *et al.*, Charge migration and charge transfer in molecular systems, *Struct. Dyn.*, 2017, **4**, 061508.
37 L. S. Cederbaum and J. Zobeley, Ultrafast charge migration by electron correlation, *Chem. Phys. Lett.*, 1999, **307**, 205–210.
38 M. Di Ventra, S. Pantelides and N. Lang, First-principles calculation of transport properties of a molecular device, *Phys. Rev. Lett.*, 2000, **84**, 979.
39 M. G. Walter, A. B. Rudine and C. C. Wamser, Porphyrins and Phthalocyanines in Solar Photovoltaic Cells, *J. Porphyrins Phthalocyanines*, 2010, **14**, 759–792.
40 M. Urbani, M.-E. Ragoussi, M. K. Nazeeruddin and T. Torres, Phthalocyanines for Dye-Sensitized Solar Cells, *Coord. Chem. Rev.*, 2019, **381**, 1–64.
41 Z. Jiang, J. Shao, T. Yang, J. Wang and L. Jia, Pharmaceutical development, composition and quantitative analysis of phthalocyanine as the photosensitizer for cancer photodynamic therapy, *J. Pharm. Biomed. Anal.*, 2014, **87**, 98–104.
42 J. Mi, L. Guo, Y. Liu, W. Liu, G. You and S. Qian, Excited-State Dynamics of Magnesium Phthalocyanine Thin Film, *Phys. Lett. A*, 2003, **310**, 486–492.
43 D. Potamianos, M. Nuber, A. Schletter, M. Schnitzenbaumer, M. Haimerl, P. Scigalla, M. Wörle, L. I. Wagner, R. Kienberger and H. Iglev, Full Dynamics Description of Mg Phthalocyanine Crystalline and Amorphous Semiconductor Systems, *J. Phys. Chem. C*, 2021, **125**, 18279–18286.
44 M. T. Hassan, T. T. Luu, A. Moulet, O. Raskazovskaya, P. Zhokhov, M. Garg, N. Karpowicz, A. Zheltikov, V. Pervak,

F. Krausz and E. Goulielmakis, Optical Attosecond Pulses and Tracking the Nonlinear Response of Bound Electrons, *Nature*, 2016, **530**, 66–70.

45 A. D. Becke, Density-Functional Exchange-Energy Approximation with Correct Asymptotic Behavior, *Phys. Rev. A: At., Mol., Opt. Phys.*, 1988, **38**, 3098.

46 A. D. Becke, Density-Functional Thermochemistry. III. The Role of Exact Exchange, *J. Chem. Phys.*, 1993, **98**, 5648.

47 C. Lee, W. Yang and R. G. Parr, Development of the Colle-Salvetti Correlation-Energy Formula into a Functional of the Electron Density, *Phys. Rev. B: Condens. Matter Mater. Phys.*, 1988, **37**, 785.

48 B. Miehlich, A. Savin, H. Stoll and H. Preuss, Results Obtained with the Correlation Energy Density Functionals of Becke and Lee, Yang and Parr, *Chem. Phys. Lett.*, 1989, **157**, 200–206.

49 M. J. Frisch, *et al.*, *Gaussian 16 Revision A.03*, Gaussian Inc., Wallingford CT, 2016.

50 D. B. Williams-Young, A. Petrone, S. Sun, T. F. Stetina, P. Lestrange, C. E. Hoyer, D. R. Nascimento, L. Koulias, A. Wildman, J. Kasper, J. J. Goings, F. Ding, A. E. DePrince III, E. F. Valeev and X. Li, The Chronus Quantum Software Package, *Wiley Interdiscip. Rev.: Comput. Mol. Sci.*, 2019, e1436.

51 J. R. Rouxel, M. Kowalewski and S. Mukamel, Current *vs.* Charge Density Contributions to Nonlinear X-ray Spectroscopy, *J. Chem. Theory Comput.*, 2016, **12**, 3959–3968.

52 J. R. Rouxel, V. Y. Chernyak and S. Mukamel, Non-local real-space analysis of chiral optical signals, *Chem. Sci.*, 2016, **7**, 6824–6831.

53 J. Campbell and T. Papp, Widths of the Atomic K–N7 Levels, *At. Data Nucl. Data Tables*, 2001, **77**, 1–56.

54 G Hermann, V Pohl, G Dixit and JC Tremblay, Probing Electronic Fluxes via Time-Resolved X-Ray Scattering, *Phys. Rev. Lett.*, 2020, **124**(1), 013002.

Supporting Information: Coherent Ring-Current Dynamics of Mg-phthalocyanine probed by Time-Resolved Circular Dichroism

Shichao Sun,* Haiwang Yong, Feng Chen, and Shaul Mukamel*

Department of Chemistry and Department of Physics & Astronomy, University of California, Irvine

E-mail: shichas2@uci.edu; smukamel@uci.edu

Contents

S1 Derivation of Time-Resolved Circular Dichroism

The electronic dynamics driven by the pump pulse is simulated by the evolution of wave function. Here we derive the TRCD signal induced by the probe pulse.

A Gaussian enveloped wave with amplitude Am, central frequency ω_c and duration σ, $W(t) = Am\, e^{-\frac{(t-T)^2}{2\sigma^2}}(e^{-i\omega_c t} + e^{i\omega_c t})$, can be expanded by frequency components $W(t) = \frac{1}{2\pi}\int_{-\infty}^{\infty} d\omega[e^{i\omega t}\tilde{W}_+(\omega) + e^{-i\omega t}\tilde{W}_-(\omega)]$, where

$$\tilde{W}_+(\omega) = Am \int_{-\infty}^{\infty} dt e^{-i\omega t} e^{-\frac{(t-T)^2}{2\sigma^2}} e^{i\omega_c t} = \sqrt{2\pi}\sigma\left[e^{-i(\omega-\omega_c)T} e^{-\frac{\sigma^2}{2}(\omega-\omega_c)^2}\right] \tag{S1}$$

$$\tilde{W}_-(\omega) = Am \int_{-\infty}^{\infty} dt e^{i\omega t} e^{-\frac{(t-T)^2}{2\sigma^2}} e^{-i\omega_c t} = \sqrt{2\pi}\sigma\left[e^{i(\omega-\omega_c)T} e^{-\frac{\sigma^2}{2}(\omega-\omega_c)^2}\right] \tag{S2}$$

The vector potential of Gaussian enveloped probe pulse with unit vector of polarization vector $\boldsymbol{\epsilon}$ can be written as

$$\begin{aligned}\mathbf{A}(\mathbf{r},t) &= \frac{1}{2\pi}\int_{-\infty}^{\infty} d\omega(\tilde{W}_-(\omega)\boldsymbol{\epsilon} e^{i(\mathbf{k}\cdot\mathbf{r}-\omega t)} + \tilde{W}_+(\omega)\boldsymbol{\epsilon}^* e^{-i(\mathbf{k}\cdot\mathbf{r}-\omega t)}) \\ &= \int_{-\infty}^{\infty} d\omega(\mathbf{A}^-(\omega,\mathbf{r},t) + \mathbf{A}^+(\omega,\mathbf{r},t))\end{aligned} \tag{S3}$$

where $\mathbf{A}^-(\omega,\mathbf{r},t) = \frac{1}{2\pi}\tilde{W}_-(\omega)\boldsymbol{\epsilon} e^{i(\mathbf{k}\cdot\mathbf{r}-\omega t)}$ and $\mathbf{A}^+(\omega,\mathbf{r},t) = \frac{1}{2\pi}\tilde{W}_+(\omega)\boldsymbol{\epsilon} e^{-i(\mathbf{k}\cdot\mathbf{r}-\omega t)}$.

With rotating wave approximation, the signal at photon frequency ω_1 is

$$S(\omega_1) = -\frac{2}{\hbar} Im \int d\mathbf{r} dt\ \langle \mathbf{j}^-(\mathbf{r},t)\cdot\mathbf{A}^+(\omega_1,\mathbf{r},t)\rangle \tag{S4}$$

To first order, from Fig. S1, with rotating wave approximation, we have first order ex-

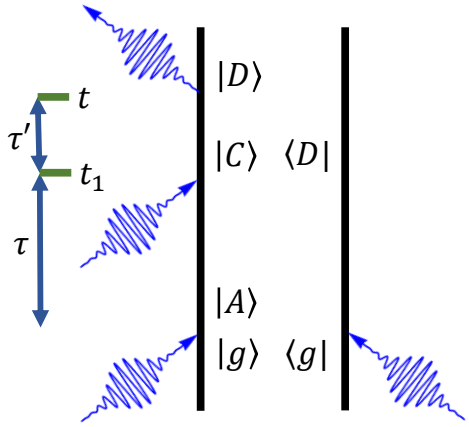

Figure S1. Ladder diagram of X-ray TRXCD. We only consider the excited state absorption contribution.

pression

$$S^{(1)}(\omega_1) = -\frac{2}{\hbar} Im \int d\mathbf{r} dt \int d\mathbf{r}_1 dt_1 d\omega_2 \left(-\frac{i}{\hbar} \langle \mathbf{j}^-(\mathbf{r},t) \cdot \mathbf{A}^+(\omega_1,\mathbf{r},t)\, \mathbf{j}^+(\mathbf{r_1},t_1) \cdot \mathbf{A}^-(\omega_2,\mathbf{r_1},t_1) \rangle \right) \tag{S5}$$

change from Heisenberg picture to Schrödinger picture,

$$S^{(1)}(\omega_1) = -\frac{2}{\hbar} Im \int d\tau d\tau' \int d\mathbf{r} d\mathbf{r}_1 \int d\omega_2 \left(-\frac{i}{\hbar} \right) \tag{S6}$$

$$\langle U^\dagger(\tau') \mathbf{j}^-(\mathbf{r}) \cdot \mathbf{A}^+(\omega_1,\mathbf{r},\tau+\tau') U(\tau) \mathbf{j}^+(\mathbf{r_1}) \cdot \mathbf{A}^-(\omega_2,\mathbf{r_1},\tau) \rangle \tag{S7}$$

expand with electronic states, the bracket expression can be expressed as

$$\begin{aligned} S^{(1)}(\omega_1) = & -\frac{2}{\hbar} Im \int d\tau d\tau' \int d\mathbf{r} d\mathbf{r}_1 \int d\omega_2 \left(-\frac{i}{\hbar} \right) \sum_{ACD} a_D^*(\tau) a_A(\tau) \langle D|U^\dagger(\tau')|D\rangle \\ & \langle D|\mathbf{j}(\mathbf{r}) \cdot \boldsymbol{\epsilon}^\dagger|C\rangle \tilde{W}_+(\omega_1) e^{i\omega_1(\tau+\tau')} e^{-i\mathbf{k}\cdot\mathbf{r}} \langle C|U(\tau')|C\rangle \langle C|\mathbf{j}^\dagger(\mathbf{r}_1) \cdot \boldsymbol{\epsilon}|A\rangle \tilde{W}_-(\omega_2) e^{-i\omega_2\tau} e^{i\mathbf{k}\cdot\mathbf{r}_1} \\ = & -\frac{2}{\hbar} Im \int d\tau d\tau' \int d\omega_2 \left(-\frac{i}{\hbar} \right) \tilde{W}_+(\omega_1) \tilde{W}_-(\omega_2) \\ & \times \sum_{ACD} a_D^*(\tau) a_A(\tau) \mathbf{j}_{DC}(\mathbf{k}) \cdot \boldsymbol{\epsilon}^\dagger\, \mathbf{j}_{CA}^\dagger(-\mathbf{k}) \cdot \boldsymbol{\epsilon} e^{i(E_D - E_C + \omega_1)\tau'} e^{-i(\omega_2-\omega_1)\tau} \end{aligned} \tag{S8}$$

where $\mathbf{k} = \frac{\omega_1}{c}\hat{\mathbf{e}}_k$. Multiplying by damping factor to account for core states (index C) decay, and integrate τ, τ',

$$S^{(1)}(\omega_1) = -\frac{2}{\hbar} Im\left(-\frac{i}{\hbar}\right) \sum_{ACD} \mathbf{j}_{DC}(\mathbf{k}) \cdot \boldsymbol{\epsilon}^\dagger \mathbf{j}^\dagger_{CA}(-\mathbf{k}) \cdot \boldsymbol{\epsilon} \int d\omega_2 \int_0^{+\infty} d\tau \int_0^{+\infty} d\tau' \\ \tilde{W}_+(\omega_1)\tilde{W}_-(\omega_2) a^*_D(\tau) a_A(\tau) e^{-i(\omega_2-\omega_1)\tau} e^{i(E_D - E_C + \omega_1)\tau'} e^{-\Gamma\tau'} \tag{S9}$$

To account for dephasing of the excited state coherences, we multiply pure dephasing factor $\exp[-\Gamma_{1,DA}\tau]$ for the coherence of excited state $A - D$, and factor $\exp[-\Gamma_{2,DC}\tau']$ for the valence-core state dephasing,

$$\begin{aligned} S^{(1)}(\omega_1) =& \frac{2}{\hbar^2} Im\, i \sum_{ACD} \mathbf{j}_{DC}(\mathbf{k}) \cdot \boldsymbol{\epsilon}^\dagger \mathbf{j}^\dagger_{CA}(-\mathbf{k}) \cdot \boldsymbol{\epsilon} \int_0^{+\infty} d\tau \int_0^{+\infty} d\tau'\, Am \\ & \tilde{W}_+(\omega_1) e^{-\frac{\tau^2 + T^2 - 2\tau(T + i\sigma^2(\omega_1 - \omega_c))}{2\sigma^2}} a^*_D(\tau) a_A(\tau) e^{-\Gamma_{1,DA}\tau} e^{i(E_D - E_C + \omega_1)\tau'} e^{-(\Gamma + \Gamma_{2,DC})\tau'} \\ =& \frac{2}{\hbar^2} Im\, i \sum_{ACD} \mathbf{j}_{DC}(\mathbf{k}) \cdot \boldsymbol{\epsilon}^\dagger \mathbf{j}^\dagger_{CA}(-\mathbf{k}) \cdot \boldsymbol{\epsilon} \frac{i}{E_D - E_C + \omega_1 + i(\Gamma + \Gamma_{2,DC})} \int_0^{+\infty} d\tau\, Am \\ & \tilde{W}_+(\omega_1) e^{-\frac{\tau^2 + T^2 - 2\tau(T + i\sigma^2(\omega_1 - \omega_c))}{2\sigma^2}} e^{-\Gamma_{1,DA}\tau} a^*_D(\tau) a_A(\tau) \\ =& -\frac{2}{\hbar^2} Im \Bigg\{ \sum_{ACD} \frac{\mathbf{j}_{DC}(\mathbf{k}) \cdot \boldsymbol{\epsilon}^\dagger \mathbf{j}^\dagger_{CA}(-\mathbf{k}) \cdot \boldsymbol{\epsilon}}{E_D - E_C + \omega_1 + i(\Gamma + \Gamma_{2,DC})} \int_0^{+\infty} d\tau\, Am \\ & \tilde{W}_+(\omega_1) e^{-\frac{\tau^2 + T^2 - 2\tau(T + i\sigma^2(\omega_1 - \omega_c))}{2\sigma^2}} e^{-\Gamma_{1,DA}\tau} a^*_D(\tau) a_A(\tau) \Bigg\} \end{aligned} \tag{S10}$$

where E_A and E_D are the energy of ground state and valence excited states, E_C is the energy of core excited states. The integral of τ is a numerical integration since $a^*_D(\tau)a_A(\tau)$ is given by the electronic dynamics.

The circular dichroism is defined as the difference of absorption of left and right circularly polarized light, $S_{CD} = S_- - S_+$. Define the polarization unit vector of circularly polarized wave as $\boldsymbol{\epsilon}_\pm(\gamma) = \frac{1}{\sqrt{2}}(\boldsymbol{\epsilon}_\alpha \pm i\boldsymbol{\epsilon}_\beta)$, where γ is the propagation direction of the wave, α, β and γ are perpendicular to each other and follow right hand rule. Specially, a wave propagating in z direction has circular polarization $\boldsymbol{\epsilon}_\pm(z) = \frac{1}{\sqrt{2}}(\boldsymbol{\epsilon}_x \pm i\boldsymbol{\epsilon}_y)$. Here the unit vector of propagation

direction vector is $\boldsymbol{\epsilon}_\kappa$, we have relation

$$\mathbf{p}\cdot\boldsymbol{\epsilon}_-^\dagger\,\mathbf{q}\cdot\boldsymbol{\epsilon}_- - \mathbf{p}\cdot\boldsymbol{\epsilon}_+^\dagger\,\mathbf{q}\cdot\boldsymbol{\epsilon}_+ = -i\mathbf{p}\times\mathbf{q}\cdot\boldsymbol{\epsilon}_\kappa$$

where $\mathbf{p}$ and $\mathbf{q}$ are arbitrary vectors.

The CD signal can be written as

$$\begin{aligned}
S_{\mathrm{CD}}(\omega_1) =& -\frac{2}{\hbar^2}Im\Bigg\{\sum_{ACD}\frac{-i\,\mathbf{j}_{DC}(\mathbf{k})\times\mathbf{j}_{CA}^\dagger(-\mathbf{k})}{E_D-E_C+\omega_1+i(\Gamma+\Gamma_{2,DC})}\cdot\boldsymbol{\epsilon}_\kappa\, Am \\
&\int_0^{+\infty}d\tau\tilde{W}_+(\omega_1)e^{-\frac{\tau^2+T^2-2\tau(T+i\sigma^2(\omega_1-\omega_c))}{2\sigma^2}}e^{-\Gamma_{1,DA}\tau}a_D^*(\tau)a_A(\tau)\Bigg\} \\
=&\frac{2}{\hbar^2}Re\Bigg\{\tilde{W}_+(\omega_1)\sum_{ACD}\frac{\mathbf{j}_{DC}(\mathbf{k})\times\mathbf{j}_{CA}^\dagger(-\mathbf{k})}{E_D-E_C+\omega_1+i(\Gamma+\Gamma_{2,DC})}\cdot\boldsymbol{\epsilon}_\kappa\, Am \\
&\int_0^{+\infty}d\tau\, e^{-\frac{\tau^2+T^2-2\tau(T+i\sigma^2(\omega_1-\omega_c))}{2\sigma^2}}e^{-\Gamma_{1,DA}\tau}a_D^*(\tau)a_A(\tau)\Bigg\} \\
=&\frac{2}{\hbar^2}Re\Bigg\{\tilde{W}_+(\omega_1)\sum_{ACD}\frac{\mathbf{j}_{DC}(\mathbf{k})\times\mathbf{j}_{CA}^\dagger(-\mathbf{k})}{E_D-E_C+\omega_1+i(\Gamma+\Gamma_{2,DC})}\cdot\boldsymbol{\epsilon}_\kappa\, Am \\
&\int_0^{+\infty}d\tau\, e^{-\frac{(\tau-T)^2}{2\sigma^2}}e^{i\tau(\omega_1-\omega_c)}e^{-\Gamma_{1,DA}\tau}a_D^*(\tau)a_A(\tau)\Bigg\}
\end{aligned}\tag{S11}$$

To avoid numerical instability, insert the definition of $\tilde{W}_+(\omega_1)$ and simplify, we have

$$\begin{aligned}
S_{\mathrm{CD}}(\omega_1) =& \frac{2(Am)^2}{\hbar^2}Re\Bigg\{\sqrt{2\pi}\sigma e^{-i(\omega_1-\omega_c)T}e^{-\frac{\sigma^2(\omega_1-\omega_c)^2}{2}} \\
&\sum_{ACD}\frac{\mathbf{j}_{DC}(\mathbf{k})\times\mathbf{j}_{CA}^\dagger(-\mathbf{k})}{E_D-E_C+\omega_1+i(\Gamma+\Gamma_{2,DC})}\cdot\boldsymbol{\epsilon}_\kappa\int_0^{+\infty}d\tau\, e^{-\frac{(\tau-T)^2}{2\sigma^2}}e^{i\tau(\omega_1-\omega_c)}e^{-\Gamma_{1,DA}\tau}a_D^*(\tau)a_A(\tau)\Bigg\} \\
=& \frac{2(Am)^2}{\hbar^2}\sqrt{2\pi}\sigma Re\Bigg\{\sum_{ACD}\frac{\mathbf{j}_{DC}(\mathbf{k})\times\mathbf{j}_{CA}^\dagger(-\mathbf{k})}{E_D-E_C+\omega_1+i(\Gamma+\Gamma_{2,DC})}\cdot\boldsymbol{\epsilon}_\kappa \\
&\int_0^{+\infty}d\tau\, e^{i(\omega_1-\omega_c)(\tau-T)}e^{-\frac{1}{2}\left[\frac{(\tau-T)^2}{\sigma^2}+\sigma^2(\omega_1-\omega_c)^2\right]}e^{-\Gamma_{1,DA}\tau}a_D^*(\tau)a_A(\tau)\Bigg\}
\end{aligned}\tag{S12}$$

In this work, the probe wave propagate in z direction. Take zero dephasing approximation,

where $\Gamma_{2,DC} = 0$ and $\Gamma_{1,DA} = 0$, and normalize by $(Am)^2$, Eq. (S12) become Eq. (3). In section S8 we will compare the effects of different dephasing factors.

S2 Valence and Core Excited States

Table S1. Excited states of Mg-phthalocyanine with nonzero oscillator strength. The transition electric dipoles $\langle g|\boldsymbol{\mu}|e\rangle$ are in atomic unit ea_0.

state	energy (eV)	$\langle g\|\mu_x\|e\rangle$	$\langle g\|\mu_y\|e\rangle$	$\langle g\|\mu_z\|e\rangle$
$1E_u$x	2.26596903	3.2204	0.0000	0.0000
$1E_u$y	2.26596903	0.0000	-3.2204	0.0000
$2E_u$x	3.36094484	-0.4366	0.0000	0.0000
$2E_u$y	3.36094484	0.0000	0.4366	0.0000
$3E_u$x	3.65324515	0.7392	0.0000	0.0000
$3E_u$y	3.65324515	0.0000	0.7392	0.0000
$4E_u$x	3.75545851	1.6162	0.0000	0.0000
$4E_u$y	3.75545851	0.0000	1.6162	0.0000
A_{2u}	3.88113308	0.0000	0.0000	0.2339
$5E_u$x	3.95713036	1.0779	0.0000	0.0000
$5E_u$y	3.95713036	0.0000	1.0779	0.0000
$6E_u$x	4.00836971	-3.1249	0.0000	0.0000
$6E_u$y	4.00836971	0.0000	3.1249	0.0000
$7E_u$x	4.49228381	3.3076	0.0000	0.0000
$7E_u$y	4.49228381	0.0000	-3.3076	0.0000

Table S2. Nitrogen K-edge core excited states of Mg-phthalocyanine. Only spin singlet states are listed.

state	irreducible representation	energy (eV)
1		386.1709
2	E_g	386.1711
3	E_g	386.1711
4		386.1713
5		386.2963
6	E_g	386.2966
7	E_g	386.2966
8		386.2972

9		386.3726
10		386.3726
11	E_g	386.3726
12	E_g	386.3726
13		386.4589
14		386.4589
15	E_g	386.4590
16	E_g	386.4590
17	B_{1u}	388.1611
18	E_g	388.1612
19	E_g	388.1612
20	A_{2u}	388.1615
21	B_{2u}	388.2934
22	E_g	388.2939
23	E_g	388.2939
24	A_{2u}	388.2946
25	B_{1u}	388.3277
26	E_g	388.3280
27	E_g	388.3280
28	A_{1u}	388.3284
29	B_{2u}	388.6100
30	E_g	388.6101
31	E_g	388.6101
32	A_{1u}	388.6103
33	A_{2u}	388.7521
34	E_g	388.7521
35	E_g	388.7521
36	B_{1u}	388.7522
37	A_{2u}	388.8027
38	E_g	388.8028
39	E_g	388.8028
40	B_{2u}	388.8029
41		389.0340
42		389.0340
43	E_g	389.0340
44	E_g	389.0340
45		389.0719
46	E_g	389.0720
47	E_g	389.0720

48		389.0720
49		389.1107
50		389.1108
51	E_g	389.1108
52	E_g	389.1108
53	A_{2u}	389.1601
54	E_g	389.1602
55	E_g	389.1602
56	B_{1u}	389.1602
57	A_{1g}	389.6734
58	E_u	389.6735
59	E_u	389.6735
60	B_{1g}	389.6738
61	A_{1g}	389.9651
62	E_u	389.9652
63	E_u	389.9652
64	B_{2g}	389.9655
65	A_{2u}	389.9825
66	E_g	389.9827
67	E_g	389.9827
68	B_{2u}	389.9830
69	A_{1u}	390.0015
70	E_g	390.0015
71	E_g	390.0015
72	B_{2u}	390.0016
73	A_{1u}	390.0205
74	E_g	390.0206
75	E_g	390.0206
76	B_{1u}	390.0208
77		390.2204
78	E_g	390.2205
79	E_g	390.2205
80		390.2208

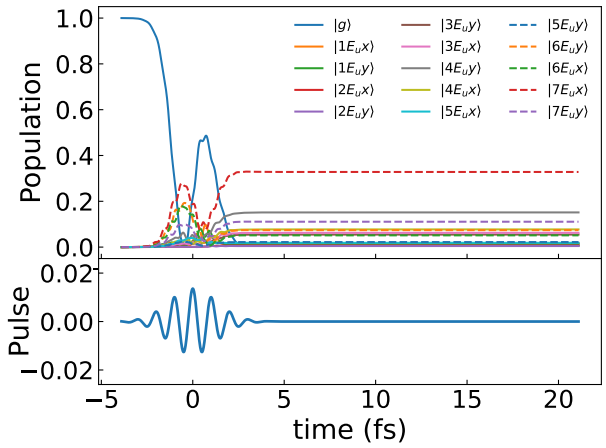

Figure S2. Population dynamics in the upper panel, pulse in the lower panel.

S3 Population Dynamics

The valence excited state population contributes to the population ring currents. After the pulse is over, the population is a constant.

S4 Mg K-edge TRXCD Spectrum

The TRXCD spectrum of Mg K-edge is displayed in Fig. S3. Due to the large core state line width of 0.45 eV, different core excited states cannot be resolved in the spectrum. We thus do not use Mg K-edge for analysis.

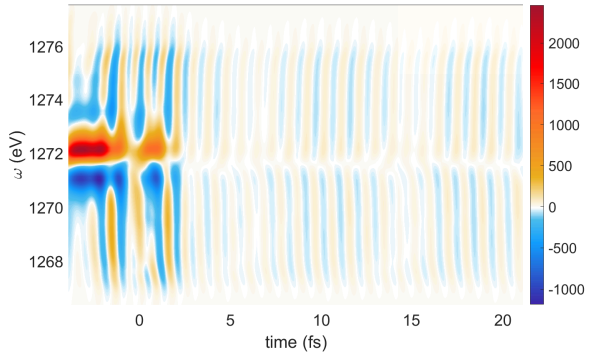

Figure S3. Time-resolved circular dichroism (Eq. 3) of Mg K-edge.

S5 Peak assignment of the CD spectrum at 10.40 fs

The Nitrogen K-edge X-ray CD spectrum at 10.40 fs is shown in Fig. S4. We assign the peaks by evaluating $\frac{\mathbf{j}_{DC}(\mathbf{k})\times\mathbf{j}^{\dagger}_{CA}(-\mathbf{k})}{E_D-E_C+\omega+i\Gamma}$ in Eq. (3).

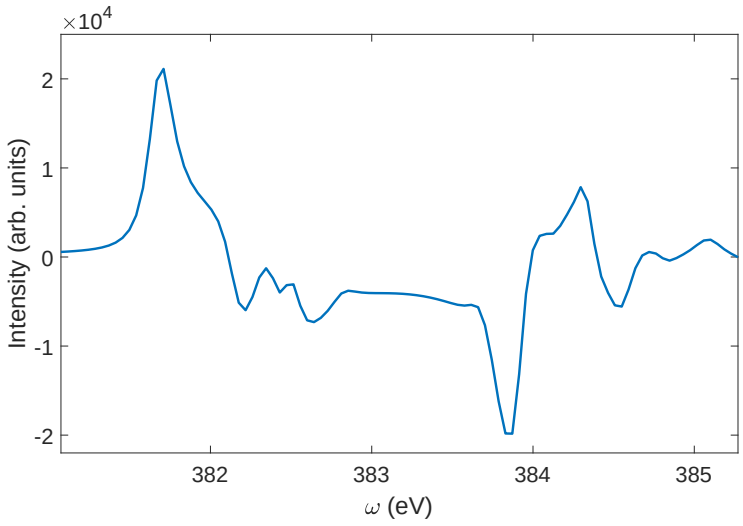

Figure S4. Nitrogen K-edge CD spectrum at 10.40 fs.

The $7E_u - 4E_u$ coherence causes 5 peaks. The peaks at 383.6690 eV and 384.4058 eV correspond to excitation to the degenerate core state 22, 23 from $7E_u$ and $4E_u$ valence state respectively. The peaks at 383.8017 eV and 384.5385 eV correspond to excitation to core state 25 from states $7E_u$ and $4E_u$ respectively. The 382.4157 eV peak represents the excitation from $4E_u$ to core states 6, 7.

The peaks at 381.6788 eV and 383.6690 eV have contributions from the excitation from $7E_u$ to degenerate core state 6, 7 and to degenerate core state 22, 23 respectively. Since they come from the $7E_u$ population, they are time-independent after the pump pulse.

The $7E_u - 6E_u$ coherence contributes to two frequencies. The peak at 381.6788 eV represents the excitation from $7E_u$ to degenerate core state 6, 7. 382.1627 eV correspond to excitation from $6E_u$ to degenerate core state 6, 7. Thus, the 382.1627 eV peak is the unique characteristic of the $7E_u - 6E_u$ coherence.

The coherence $7E_u - 1E_u$ contributes to two frequencies. Peak at 381.6788 eV excitation

from $7E_u$ to core state 6, 7. at 383.9051 eV is excitation from $1E_u$ to core state 6, 7. So, the 383.9051 is the characteristic peak of this coherence.

The coherence $7E_u - 5E_u$ corresponds to 4 peaks. 383.8017 eV is excitation from $7E_u$ to core state 25. 384.3369 eV is from $5E_u$ to core state 25. 383.6690 eV is from $7E_u$ to core state 22. 384.2041 eV is from $5E_u$ to core state 22. Thus 384.3369 and 384.2041 eV are the characteristic peaks of this coherence.

The $7E_u - 3E_u$ coherence has two peaks. 381.6788 eV is the excitation from $7E_u$ to core state 6, 7. 382.5179 eV is excitation from $3E_u$ to core state 6, 7. Thus, 382.5179 eV is the characteristic peak.

The $6E_u - 1E_u$ coherence has two peaks. 382.1627 eV, is the excitation from $6E_u$ to core state 6, 7. 383.9051 eV is from $1E_u$ to core state 6, 7. They share the same energy range as other coherence.

The $4E_u - 1E_u$ coherence has two peaks. 382.4157 eV is excitation from $4E_u$ to core state 6, 7. 383.9051 eV is excitation from $1E_u$ to core state 6, 7.

The $4E_u - 3E_u$ coherence has two peaks. 382.4157 eV is from $4E_u$ to core state 6, 7. 382.5179 eV is from $3E_u$ to core state 6, 7.

Coherence $5E_u - 1E_u$ has two peaks. 382.2140 eV is $5E_u$ to core state 6, 7. 383.9051 eV is from $1E_u$ to core state 6, 7. So 382.2140 eV is characteristic.

The peak assignment to specific coherences, the oscillation periods and the coherence frequencies are summarized in Table 2 in the main text.

S6 The Induced Magnetic Field

The induced magnetic field created by ring current can indicate the direction and strength of ring current. We use Biot-Savart law to caclculate the induced magnetic field at the center of the molecule (on Mg atom) as a function of time. Assume the molecule is in the plane of paper, z direction is pointing out of the paper to the reader, a counter-clockwise current

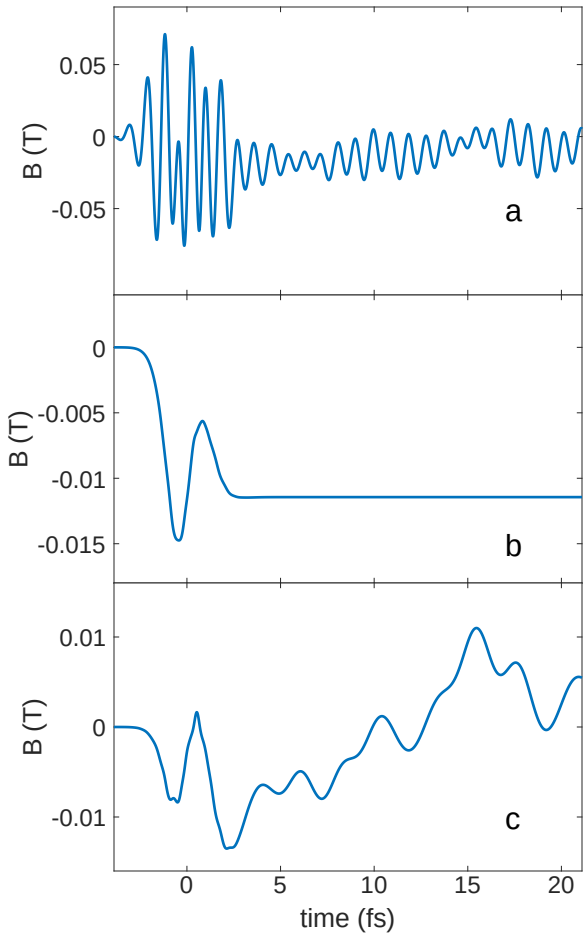

Figure S5. Time-resolved induced magnetic field. Panel a is the total induced magnetic field. Panel b is the contribution from the population ring current. After the pump pulse finish, their contribution becomes constant at -0.01144 T. Panel c is the contribution from the coherent ring current from the coherence between excited states.

will create induced magnetic field pointing into the paper, which is negative valued while the clockwise current create positive valued induced magnetic field pointing out of the paper.

The time evolution of induced magnetic field by ring current is displayed in Fig. S5. The total induced magnetic field include the contribution from population ring current, g-ex coherent current and ex-ex coherence between states with different energy. The fast oscillation in panel a is contributed by g-ex coherence due to their relatively large energy separation. The contribution from the population ring current is displayed in panel b. After the pulse, their contribution become a constant at -0.01144 T. The contribution from the

ex-ex coherent ring current is displayed in panel c.

S7 Decomposition of Induced Magnetic Field

We decompose the ex-ex coherent ring current into individual coherence pair in Fig. S6.

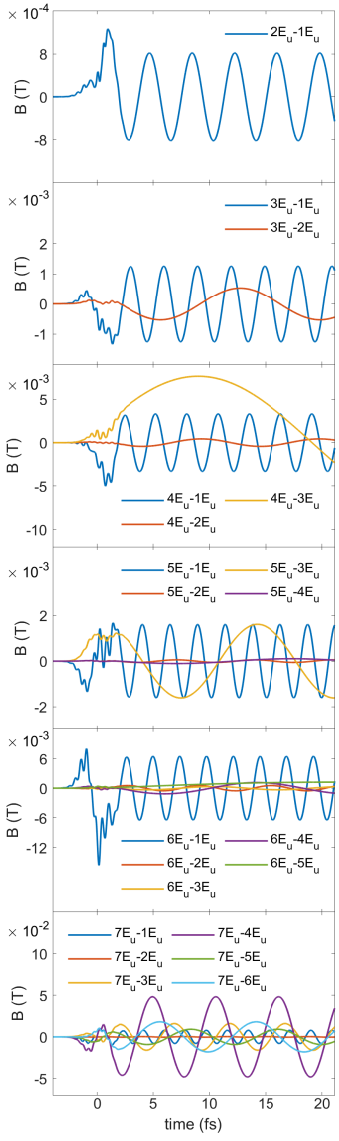

Figure S6. Contribution of the excited states coherence to the induced magnetic field.

S8 TRXCD Spectrum with Pure Dephasing

In Eq. (S12), the effect of dephasing is added as pure dephasing to describe the decoherence induced by the interaction between the molecular system with bath. The factor $e^{-\Gamma_{1,DA}\tau}$ gives rise to the decoherence of valence-valence state coherence, where index D, A run over ground and valence excited states. As will be shown in the result, the ground state-valence excited state coherence does not contribute to any change, since the coherence between ground state and valence state has a shorter oscillation period than the pulse duration, thus not observable in the time-resolved spectra. The parameter $\Gamma_{2,DC}$ give rise to the decoherence of valence-core state coherence. TRXCD spectra and their Fourier transformed spectra with different pure dephasing strength are displayed in Fig. S7. For $\Gamma_{1,DA}$ and $\Gamma_{2,DC}$ equal to $1/100$ fs^{-1}, the results are similar to no dephasing results. As the dephasing parameter increase, the TRXCD signal decay with time. Larger dephasing corresponds to earlier decay. As a result, in Fourier transformed spectra, as the dephasing parameters increase, the strength of the peaks decrease, so does the peak resolution in frequency axis ($\hbar\omega'$). Aside from that, as in Eq. (S12), $\Gamma_{2,DC}$ in the denominator will broaden the peak in energy domain. Since the value of dephasing parameter is smaller than the life time decay Γ of core excited states, this broadening is not significant.

S9 Calculation of Local Ring Current

Local ring currents are calculated by numerically integrating the current density at a plane, $I = \int_A dS\, \hat{\mathbf{n}} \cdot \mathbf{j}$, where $\mathbf{j}$ is the current density, A is the plane, $\hat{\mathbf{n}}$ is the normal vector of the plane. As depicted in Fig. S8, different plane and normal vectors are chosen for different zones. Mg atom is at the origin, with x and y axis shown in Fig. S8.

For ring α, the plane is chosen as half plane in xz plane, with boundary going through the center of benzene ring α and perpendicular to xy plane. The normal vector is the unit vector in $-y$ direction. The integration of current density in this plane gives the current

going in $-y$ direction through this plane, i.e., the current I of ring α, see top panel of Fig. 4. Similarly, the integration plane of ring γ is the half plane in xz plane, with its boundary going through the center of benzene ring γ, with normal vecor in $+y$. Positively valued $I(\alpha)$, $I(\gamma)$ indicates clockwise ring currents in ring α, γ.

The integration plane for ring β and δ are half plane in yz plane, with their boundary going through the center of benzene ring β and δ respectively. The normal vectors of β is in $-x$ direction while the normal vector for δ is in $+x$. Positively valued $I(\beta)$ and $I(\delta)$ indicates clockwise ring currents in ring β and δ respectively.

The integration plane for ring current around Mg atom (CT) is in xz plane between the Mg nucleus and the middle point of Mg and N, as the black line in Fig. S8. The normal vector is in $-y$. Positive I(CT) indicates clockwise CT ring current. Similar to CT, the integration plane for outer ring (OT) current is in xz plane between x = 3.4 Å and the middle point of Mg and N (the orange line in Fig. S8). The normal vector is in $-y$. Positive I(OT) indicates clockwise OT ring current.

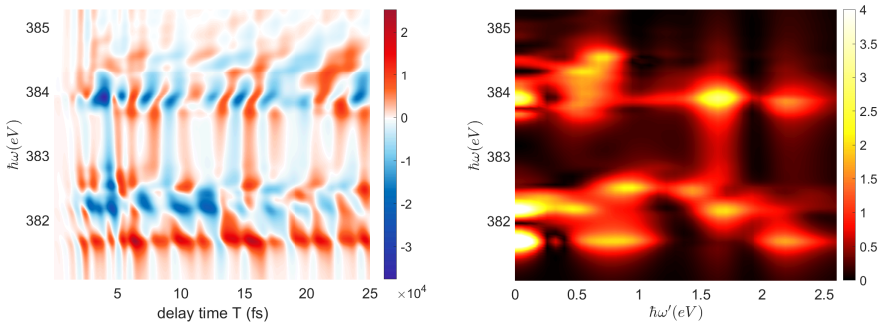

Figure S7.1. Dephasing parameters $\Gamma_{1,DA}$ and $\Gamma_{2,DC}$ both set to $1/100$ fs^{-1}.

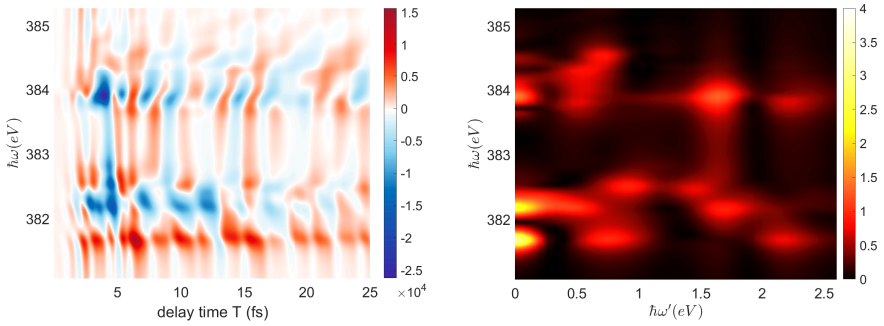

Figure S7.2. Dephasing parameters $\Gamma_{1,DA}$ and $\Gamma_{2,DC}$ both set to $1/20$ fs^{-1}.

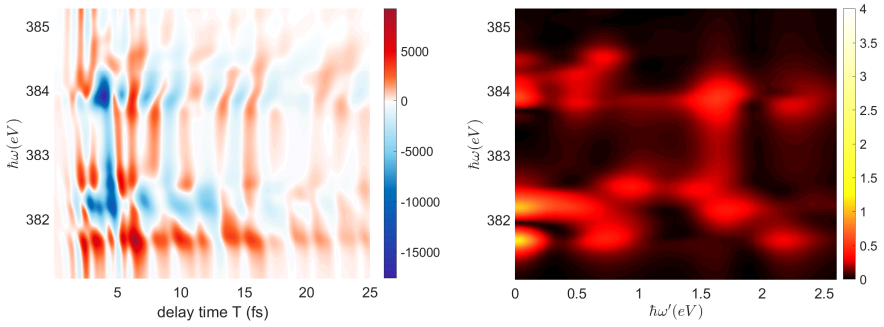

Figure S7.3. Dephasing parameters $\Gamma_{1,DA}$ and $\Gamma_{2,DC}$ both set to $1/10$ fs^{-1}.

Figure S7. Dephasing parameters $\Gamma_{1,DA}$ and $\Gamma_{2,DC}$ both set to $1/100$ fs^{-1}, $1/20$ fs^{-1} and $1/10$ fs^{-1} respectively. Left panels are TRXCD spectra, right panels are the Fourier transformed spectra. Arbitrary units are used with the same scale.

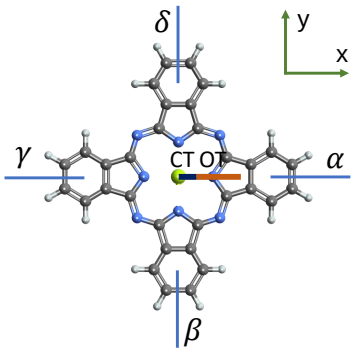

Figure S8. The integration planes for calculating the local ring currents in different zones of the molecule.